



Deposited via The University of Leeds.

White Rose Research Online URL for this paper:

<https://eprints.whiterose.ac.uk/id/eprint/182605/>

Version: Accepted Version

Article:

Liu, Y, Wu, S, Fan, C et al. (2023) Variations in surface functional groups, carbon chemical state and graphitization degree during thermal deactivation of diesel soot particles. *Journal of Environmental Sciences*, 124. pp. 678-687. ISSN: 1001-0742

<https://doi.org/10.1016/j.jes.2022.01.007>

© 2022 The Research Center for Eco-Environmental Sciences, Chinese Academy of Sciences. Published by Elsevier B.V. This manuscript version is made available under the CC-BY-NC-ND 4.0 license <http://creativecommons.org/licenses/by-nc-nd/4.0/>.

Reuse

This article is distributed under the terms of the Creative Commons Attribution-NonCommercial-NoDerivs (CC BY-NC-ND) licence. This licence only allows you to download this work and share it with others as long as you credit the authors, but you can't change the article in any way or use it commercially. More information and the full terms of the licence here: <https://creativecommons.org/licenses/>

Takedown

If you consider content in White Rose Research Online to be in breach of UK law, please notify us by emailing eprints@whiterose.ac.uk including the URL of the record and the reason for the withdrawal request.

Variations in surface functional groups, carbon chemical state and graphitization degree during thermal deactivation of diesel soot particles

Ye Liu^{a*}, Sijin Wu^a, Chenyang Fan^{b*}, Xin Wang^b, Fangjie Liu^b, Haibo Chen^a

^a Institute for Transport Studies, University of Leeds, Leeds LS2 9JT, UK

^b Vehicle & Transportation Engineering Institute, Henan University of Science and Technology, Luoyang 471003, China

Abstract: The thermal deactivation of diesel soot particles exerts a significant influence on the control strategy for the regeneration of diesel particulate filters (DPFs). This work focused on the changes in the surface functional groups, carbon chemical state, and graphitization degree during thermal treatment in an inert gas environment at intermediate temperatures of 600 °C, 800 °C, and 1000 °C and probes the reason for thermal deactivation. The surface functional groups and carbon chemical state were characterized using Fourier transform infrared spectroscopy (FT-IR) and X-ray photoelectron spectroscopy (XPS). The graphitization degree was evaluated by means of Raman spectroscopy (RS). The concentrations of aliphatic C–H, C–OH, C=O, and O–C=O groups are reduced for diesel soot and carbon black when increasing the thermal treatment temperature, while the sp^2/sp^3 hybridized ratio and graphitization degree enhance. These results provide comprehensive evidence of the decreased reactivity of soot samples. Among oxygenated functional groups, the percentage reduction during thermal treatment is the largest for the O–C=O groups owing to its worst thermodynamic stability.

Keywords: Diesel soot particles; Surface functional groups; Carbon chemical state; graphitization degree; Thermal deactivation

20 **1. Introduction**

21 Currently, diesel particulate filters (DPFs), as a common technology, are widely employed to reduce
22 soot particle emissions and improve air quality (Schejbal et al., 2009). In DPFs, soot particles are trapped
23 until these soot particles will be oxidized when DPF regeneration takes place. The high-temperature
24 exhaust gases varying from 250 to 850 °C during this process pass continuously through DPFs (Roth et
25 al., 1998; Matsumoto et al., 2008; Raj et al., 2014). These trapped soot particles undergo thermal treatment
26 for a long time in DPFs, which inevitably causes the thermal deactivation of diesel soot particles. Thermal
27 deactivation means a reduction in reactivity upon thermal treatment (Vander Wal et al., 2004; Sheng,
28 2007), making diesel soot particles more resistant to be removed when the DPFs regenerate. Thus, it is
29 necessary to probe the reason behind the thermal deactivation to further optimize the control strategy for
30 the DPF regeneration.

31 Many studies have been conducted concerning the thermal deactivation of carbonaceous materials
32 such as coal char, carbon black, and soot particles (Feng et al., 2002; Sheng, 2007; Raj et al., 2014;
33 Jaramillo et al., 2015). For instance, Feng et al., (2002) studied the impact of thermal treatment in the
34 850 °C–1150 °C range on the structure and reactivity of the coal char. The results indicated that the
35 thermal deactivation was strongly dependent on the crystallite-perfecting process during thermal
36 treatment. The same conclusions were reached by Sheng (2007), who reported that the increased
37 structural ordering of char crystalline during thermal treatment between 1200 °C and 1500 °C was
38 responsible for the thermal deactivation. Gaddam et al., (2016) studied the variation in the nanostructure
39 and reactivity of the model carbons when heated to a temperature up to 3000 °C under a He atmosphere.
40 The crystallite growth and increase in density during thermal treatment were observed, which caused the

41 decreased reactivity. Jaramillo et al., (2015) explored the changes in nanostructure and reactivity of three
42 model carbons during oxidation at temperatures in the range of 575 °C –775 °C in air. The results
43 presented a good relationship between oxidative reactivity and carbon nanostructure. Zolin et al., (2002)
44 analysed the influence of thermal treatment in an oxygen environment on oxidative reactivity of coal char
45 and found that the elimination of hydrogen and oxygen in the carbonaceous matrix and loss of edge active
46 sites during thermal treatment would lead to a reduction in the oxidative reactivity. However, limited
47 information regarding the changes in the surface functional groups, carbon chemical state, and
48 graphitization degree of diesel soot particles during thermal deactivation is available in a nitrogen
49 environment at temperatures ranging from 600 °C to 1000 °C. Although the exhaust gases passing through
50 a DPF include several gas components, the nitrogen is approximately 70 % or even more in these gases
51 Reşitoğlu et al., (2014). Moreover, the thermal treatment performed under only nitrogen conditions would
52 eliminate the effect of other gas components on the experimental results.

53 Surface functional groups bonded to non-six-membered carbon rings during the soot oxidation
54 process exert a crucial influence on soot structure and reactivity (Santamaria et al., 2006; Vander Wal et
55 al., 2007). The thermal decomposition of these functional groups would chemically and physically
56 weaken the barriers to lamella reorganization, favouring the rearrangement of carbon lamella and
57 changing the nanostructure (Vander Wal et al., 2007). Simultaneously, the preferential loss of surface
58 functional groups can enhance reactive sites, thereby increasing the soot reactivity (Agudelo et al., 2014;
59 Soriano et al., 2017; Xu et al., 2019). The sp^2 and sp^3 hybridized carbon atoms are primarily chemical
60 states in soot, and the relative amount and spatial relationships are closely associated with the soot
61 structure and reactivity (Vander Wal et al., 2016). In addition, the degree of graphitization is a vital

62 indicator of soot structural order, which is strongly associated with the in-plane crystallite size, affecting
63 soot reactivity (Sheng, 2007; Liu et al., 2017; Zhou et al., 2022).

64 In this context, the purpose of the present work is to study the alterations in surface functional groups,
65 carbon chemical state and graphitization degree during thermal treatment of soot samples in an inert gas
66 atmosphere at temperatures ranging from 600 to 1000 °C and further explore the reason for thermal
67 deactivation. The carbon chemical state and surface functional groups were characterized by means of X-
68 ray photoelectron spectroscopy (XPS) and Fourier transform infrared spectroscopy (FT-IR). The
69 graphitization degree of soot particles was evaluated using Raman spectroscopy (RS).

70 **2. Experimental setup**

71 2.1. Soot samples

72 Diesel soot particles were sampled on Teflon filters (R2PL047, PALL, USA) from a four-cylinder,
73 four-stroke and turbo-charged compression ignition diesel engine. Table 1 lists the details of the engine
74 used. The engine operating load and speed were set at 55% of the full load and 1800 rpm. The soot
75 samples were scraped from the filters after sampling for further thermal treatment. Additionally, the
76 Printex-U, a commercial carbon black from Evonik-Degussa, was also examined to compare the
77 properties of the diesel soot and Printex-U because the Printex-U is frequently employed as a surrogate
78 for diesel soot (Vander Wal et al., 2007; Raj et al., 2013).

79

80

81

82

83 **Table 1.** Detailed specifications of the diesel engine

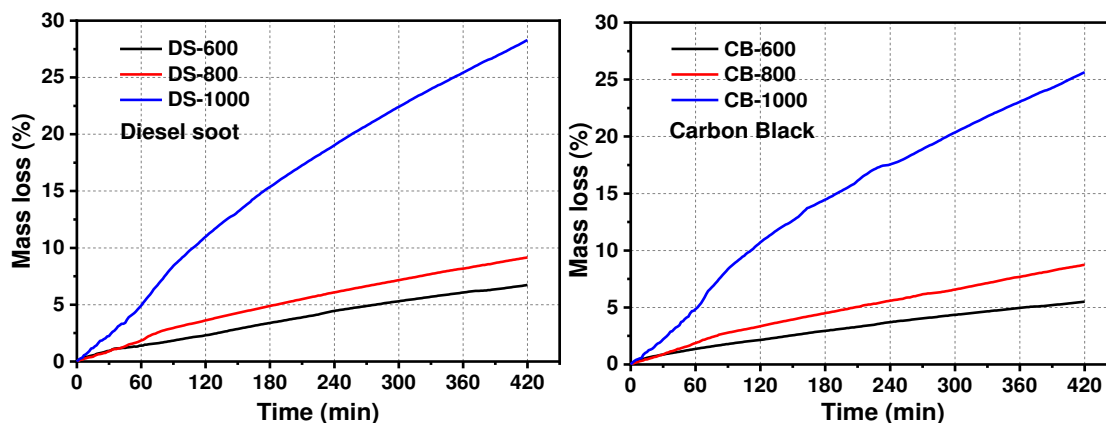
Engine parameters	
Number of cylinders, configuration	Four, in-line
Bore×stroke (mm)	102×108
Compression ratio	17:1
Engine displacement (L)	3.856
Rated power	100 kW@2800 rpm
Maximum torque (N·m)	420
Fuel injection type	Common rail system

84 2.2. Thermal treatment

85 For each thermal treatment, 5 mg of the soot sample in platinum crucibles of TGA was performed
86 under a nitrogen atmosphere. The nitrogen environment chosen for thermal treatment is because the
87 nitrogen is approximately 70 % or even more in the exhaust gases passing through a DPF (Reşitoğlu et
88 al., 2014). Moreover, the thermal treatment performed under only a nitrogen environment would isolate
89 the effect of other gas components of exhaust gases on experimental results. Previous studies have
90 demonstrated that thermal treatment at 450 °C for 60 min under an inert gas condition could effectively
91 remove the absorbed unburned hydrocarbons and volatile matters and exert a limited influence on soot
92 properties (Yehliu et al., 2012; Yehliu et al., 2013). Thus, the temperature was heated to 450 °C at first
93 and kept this temperature for 60 min. The diesel soot and carbon black after the removal of these volatile
94 matters were termed DS-D and CB-D. Then the isothermally thermal treatment was carried out under
95 various temperatures for seven hours. The significant thermal deactivation occurs when the thermal
96 treatment temperature is above 500 °C in an inert gas condition (Raj et al., 2014; Gaddam et al., 2016).
97 Consequently, 600 °C, 800 °C, and 1000 °C were chosen as isothermal thermal treatment temperatures
98 to study the variations in soot properties during the thermal deactivation of soot particles. The diesel soot
99 and carbon black after thermal treatment at 600 °C, 800 °C, and 1000 °C are denoted as DS-600, DS-800,

100 DS-1000, CB-600, CB-800, and CB-1000, respectively.

101 The mass loss of diesel soot and carbon black against the treatment time under various temperatures
102 is shown in Fig.1. There is a slight mass loss for both diesel soot and carbon black at 600 °C. The mass
103 loss for the diesel soot and carbon black all reaches about 9% at 800 °C, while the mass loss at 1000 °C
104 is observed to be up to 28.3 % for diesel soot and 25.6 % for carbon black. Such a mass loss of soot
105 samples is likely to be associated with thermal fragmentation and the decomposition of oxygenated
106 compounds (Chung and Violi, 2011; Wang, 2011; Raj et al., 2014). The occurrence of thermal
107 fragmentation causes the sublimation of small polycyclic aromatic hydrocarbons (PAHs) on the surface
108 of soot samples. On the other hand, the oxygenated compounds existing in soot samples would be
109 desorbed when heated above 500 °C (Song et al., 2006; Raj et al., 2014).



110

111 **Fig. 1.** Mass loss of soot samples during thermal treatment at various temperatures (Liu et al., 2022).

112 2.3. FT-IR

113 FT-IR was used to identify and quantify the surface functional groups on the soot surface. FT-IR
114 spectrometer (Nicolet Nexus 470) was employed with a spectral range of 600–3200 cm^{-1} and a resolution
115 of 1 cm^{-1} . The soot samples and analysis grade KBr (0.5 wt%) were mixed and ground, and mixed

116 dispersions were compressed for 5 min at 10 Ton into a thin disk.

117 2.4. XPS

118 XPS was implemented to acquire information on the oxygenated functional group and the carbon
119 chemical state in the soot samples. A PerkinElmer PHI-1600 ESCA spectrometer was employed to record
120 XPS spectra using an Mg K α X-ray source operated at ultra-high vacuum conditions. The C1s peak of
121 contaminant carbon (BE=284.6 eV) was served as an internal standard to calibrate the binding energies.
122 More than three spectra for each sample were obtained to make sure the reproducibility of the tested
123 results.

124 2.5. RS

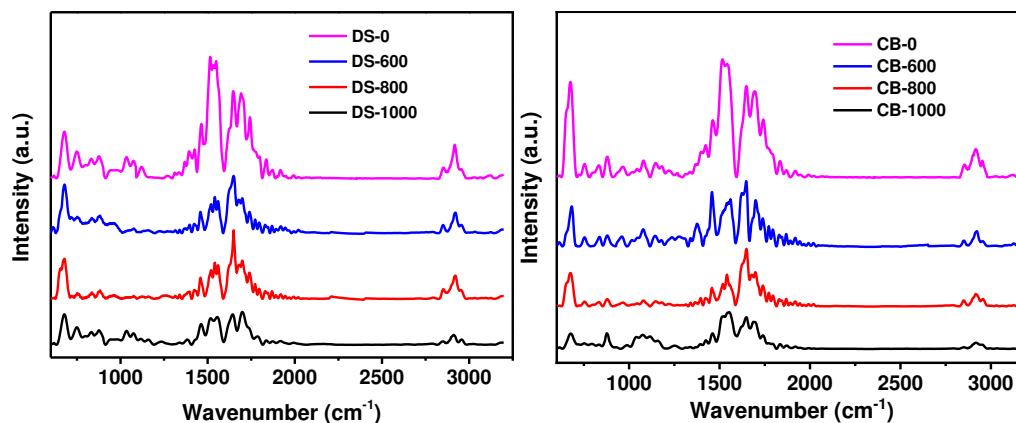
125 Raman spectra were measured by means of Raman microscope system (Renishaw 1000) with and a
126 wavelength of 514.5 nm and an Ar ion excitation laser. Raman spectra in the 900–2000 cm⁻¹ range were
127 recorded with an exposure time of 60 s. About 1 mW laser beam power was employed to avoid modifying
128 or burning the soot samples. For each sample, more than three spectra were obtained to make sure the
129 reproducibility of the results.

130 3. Results and discussion

131 3.1. Surface functional groups

132 In the present study, FT-IR was used to identify and quantify the surface functional groups on the
133 soot surfaces. Fig. 2 shows the background-corrected, smoothed FT-IR spectra of diesel soot and carbon
134 black over thermal treatment at various temperatures in the region between 600 and 3200 cm⁻¹. All the
135 soot samples have almost similar positions of peaks but exhibit different signal intensities. Three well-
136 defined aliphatic CH₃ asymmetric stretching, CH₂ asymmetric stretching and CH₃ symmetric stretching

137 peaks are measured at 2960, 2920, and 2850 cm^{-1} , respectively, which are primarily from methylene
138 bridges maintaining the interconnection among PAHs or from methyl, methylene, and methine attached
139 to aromatic rings on PAHs (Ibarra et al., 1996; Santamaria et al., 2006; Liu et al., 2016). The aliphatic C–
140 H plane deformations of CH_2/CH_3 groups are measured and located at 1380 and 1450 cm^{-1} , respectively
141 (Santamaria et al., 2006; Cain et al., 2010). Most of the peaks detected here are also observed for soot
142 particles formed in an inverse diffusion flame (Santamaria et al., 2006; Santamaria et al., 2010). However,
143 no signal of aromatic C–H stretching located at around 3030 cm^{-1} is measured in this study. The aromatic
144 out-of-plane C–H bending vibrations of three-adjacent, two-adjacent and isolated hydrogens are observed
145 at 750, 830, and 880 cm^{-1} , respectively (Santamaria et al., 2006; Russo et al., 2014). The peak at 675 cm^{-1}
146 is measured in this study, which is assigned to aromatic out-of-plane C–H bending vibration (Bladt et
147 al., 2012). In addition, the peaks at 1640 and 1520 cm^{-1} are detected, corresponding to the stretching of
148 alkenyl C=C and aromatic C=C–C groups (Santamaria et al., 2006; Raj et al., 2014). Some oxygen-related
149 functional groups are also measured for the soot samples. The peak of C=O stretching of carboxylic
150 groups is observed at about 1700 cm^{-1} (McKinnon et al., 1996; Kirchner et al., 2000). The oxygen-carbon
151 stretching groups of the ether, esters and hydroxyl appear at 1260, 1100, and 1050 cm^{-1} , respectively
152 (Cain et al., 2010).



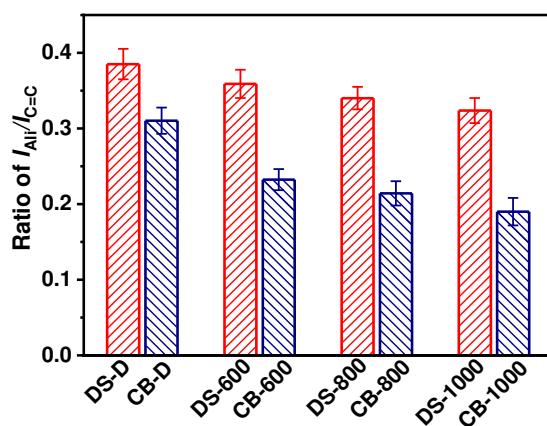
153
154 **Fig. 2.** FT-IR spectra of diesel soot and carbon black over thermal treatment at various temperatures.

155 *3.1.1. Aliphatic and aromatic C–H groups*

156 Given some factors, such as the content and thickness of the KBr pellet, have an impact on the signal
157 intensity in FT-IR spectra, the intensity ratio of the aliphatic C–H peak at 2920 cm^{-1} to the aromatic C=C
158 peak at 1640 cm^{-1} ($I_{\text{Al}}/I_{\text{C=C}}$) is used to quantify the relative concentration of aliphatic C–H groups in the
159 light of the suggestion by McKinnon et al., (1996) and Santamaría et al., (2007). Fig. 3 presents the
160 variation in the $I_{\text{Al}}/I_{\text{C=C}}$ ratios as functions of thermal treatment temperatures. The diesel soot and carbon
161 black exhibit the same evolution trend regarding changes in the $I_{\text{Al}}/I_{\text{C=C}}$ ratios when increasing thermal
162 treatment temperature. The relative content of aliphatic C–H groups reduces gradually with an increase
163 in thermal treatment temperature, indicating that the higher thermal treatment temperature would
164 consume more aliphatic hydrogen. This behavior is primarily ascribed to the following factors: (1) the
165 increased carbonization reactions with increasing thermal treatment temperatures enhance
166 dehydrogenation rates (Wang et al., 2013; Liu et al., 2016); (2) the more cyclic or acyclic aliphatics
167 including aliphatic C–H groups would be desorbed from soot surfaces when heated at higher thermal
168 treatment temperature (Raj et al., 2014). In the study of the soot carbonization process by Vander Wal

169 (1998), it was found that carbonization reduced the concentration of hydrogen functional groups. Dobbins
170 et al., (1995, 1996) stated that the carbonization reaction would reduce aliphatic C–H functional groups
171 on soot surfaces.

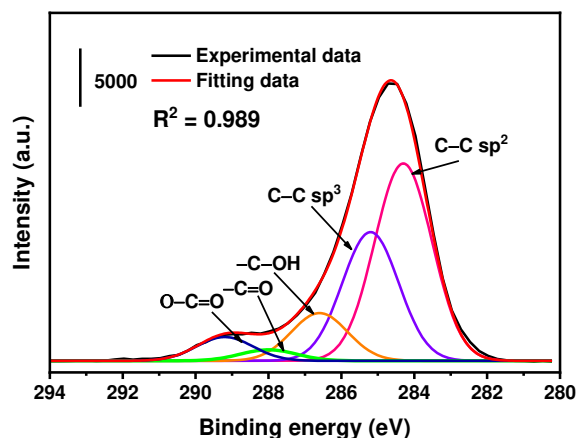
172 Aliphatic C–H groups are a crucial factor affecting soot oxidation reactivity (Wang et al., 2013). The
173 abstraction of H-atoms in aliphatic C–H groups requires lower energy, and the preferential loss of
174 aliphatic hydrogen enhances the number of active sites, increasing soot reactivity (Santamaria et al., 2006).
175 As a result, the concentration of aliphatic C–H functional groups reduces when increasing thermal
176 treatment temperature, which decreases the number of active sites and lowers soot reactivity. Agudelo
177 et al., (2014) investigated the soot particles from diesel and crude vegetable oils. The results presented
178 that the reduction in aliphatic C–H groups led to the decreased reactivity. The same conclusion was
179 reached by Ruiz et al., (2015), who found that the soot reactivity reduced as the concentration of aliphatic
180 C–H groups decreased. Soriano et al., (2017) discovered that soot generated from paraffinic fuel had
181 higher reactivity than that from diesel fuel. They revealed that this higher reactivity was due to a higher
182 concentration of aliphatic functional groups.



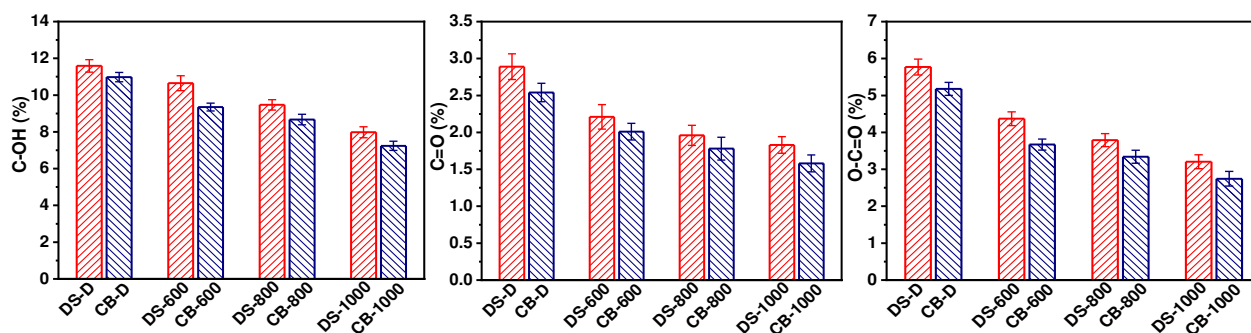
183
184 **Fig. 3.** Relative concentrations of aliphatic C–H functional groups as functions of thermal treatment temperature.

185 3.1.2. Oxygenated functional groups

186 XPS analyses in this study were carried out to gain information regarding the oxygenated functional
187 groups and carbon chemical state. Fig. 4 presents a representative high-resolution scan of the C1s peak.
188 The C1s region was deconvoluted to four peaks according to the method suggested in the literature
189 (Pumera and Iwai, 2009; Gaddam and Vander Wal, 2013): the peak at 286.6 eV assigned to hydroxyl (C–
190 OH) groups, the peak at 288.4 eV corresponding to carbonyl (C=O) group, and the peak at 289.2 eV
191 referring to the carboxylic acid (O–C=O) group. The analysis of sp^2 and sp^3 hybridized carbons will be
192 discussed in detail in the subsequent section. The concentrations of C–OH, O–C=O and C=O groups for
193 diesel soot and carbon black are plotted against thermal treatment temperatures in Fig. 5. The contents of
194 C–OH, O–C=O and C=O groups reduce when increasing the thermal treatment temperature, indicating
195 that the more oxygenated functional groups are desorbed at the higher temperature. According to previous
196 work (Song et al., 2007; Lapuerta et al., 2020), the oxygenated groups are important intermediate
197 compounds and exert a crucial influence on oxidation reaction, influencing soot reactivity. In the present
198 work, the oxygenated functional groups for soot samples decrease with the increase in thermal treatment
199 temperature, which in turn reduced soot reactivity. Song et al., (2006) probed the correlation between the
200 oxygenated functional groups and reactivity and found that the decreased relative concentration of
201 oxygenated functional groups would reduce soot reactivity. Soriano et al., (2017) came to the same
202 conclusion, and the results revealed that the biodiesel soot possessed higher concentrations of oxygenated
203 functional groups compared to diesel soot and had higher oxidative reactivity. However, a different
204 conclusion was obtained by Yehliu et al., (2012), who found that the content of oxygenated functional
205 groups was not associated with soot reactivity.



206
207 **Fig. 4.** Representative XPS C 1s narrow spectra for DS-D



208
209 **Fig. 5.** Contents of C–OH, O–C=O and C=O groups as functions of thermal treatment temperature.

210 The percentage reductions of C–OH, C=O and O–C=O groups for diesel soot and carbon black are
 211 calculated with various thermal treatment temperatures. Compared to DS-D, the concentrations of C–OH,
 212 C=O and O–C=O groups for DS-1000 reduce by 31%, 37%, and 44%. Similarly, the contents of C–OH,
 213 C=O and O–C=O groups for CB-1000 decrease by 34%, 38% and 47% than those for CB-D. The
 214 percentage reduction for diesel soot and carbon black follows the sequence: O–C=O > C=O > C–OH
 215 groups, which is likely to be correlated with the relative thermodynamic stability of these oxygenated
 216 functional groups. In the study by Vander Wal et al., (2010), it was discovered that the relative
 217 thermodynamic stability of C–OH, C=O and O–C=O groups decreases sequentially. As a result, the O–
 218 C=O groups have the worst thermodynamic stability, and thus the percentage reduction is the largest for

219 the O–C=O groups.

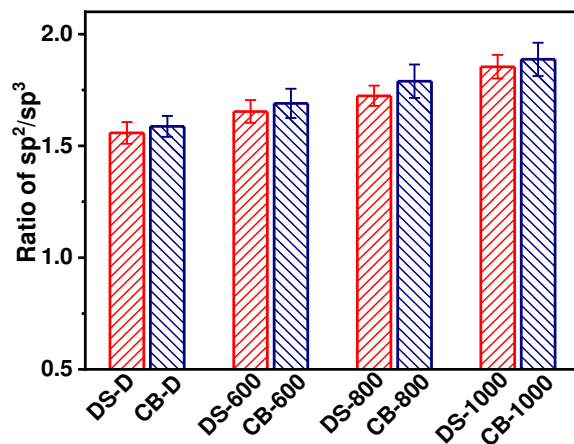
220 3.2. Carbon chemical state

221 XPS was also used to gain chemical information regarding the sp^2 and sp^3 hybridized carbon atoms
222 (Tandon and Rosner, 1996; Vander Wal et al., 2014). The sp^2 and sp^3 hybridized carbon atoms are integral
223 to the overall soot nanostructure. As shown in Fig. 4, the deconvolution of the high-resolution spectrum
224 about the C1s region was performed to quantify the relative contents of sp^2 and sp^3 hybridized carbon
225 atoms. The peak near 284.3 eV is a representation of sp^2 hybridized carbons and π bonding in soot (Raj
226 et al., 2014; Guerrero Peña et al., 2016). The peak near 285.2 eV is assigned to the sp^3 hybridized carbons
227 and σ bonding in soot (Raj et al., 2014; Guerrero Peña et al., 2016). The sp^2 hybridized carbons refer to
228 the ordered carbon, and the sp^3 hybridized carbon atoms would affect the sp^2 hybridized network and
229 need bond terminations other than adjacent π bonded carbon atoms. These sp^3 hybridized carbon atoms
230 would reduce the structural order and are consequently considered as the defect sites (Vander Wal et al.,
231 2011). Thus, a large sp^2/sp^3 hybridization ratio corresponds to a more ordered structure (Alfe et al., 2009).

232 Fig. 6 shows the sp^2/sp^3 values for diesel soot and carbon black as functions of thermal treatment
233 temperature. Compared to diesel soot, carbon black has slightly larger sp^2/sp^3 values at each thermal
234 treatment temperature. In addition, a monotonic increase trend in sp^2/sp^3 hybridization ratios for diesel
235 soot and carbon black is observed with increasing thermal treatment temperature, demonstrating that soot
236 samples transform towards a more ordered structure as thermal treatment temperature increases. This
237 behavior is primarily due to the desorption of more amorphous species on soot surfaces when increasing
238 thermal treatment temperature. Raj et al., (2014) also reported that amorphous and disorder species were

239 desorbed from soot surfaces, which included a large quantity of cyclic or acyclic aliphatics. In the study
240 by Fetzer (2000), it was found that some amorphous PAHs making up soot particles would be sublimated
241 at approximately 500 °C. Consequently, more amorphous PHAs will be sublimated when heated above
242 500 °C, which favours soot samples towards a better graphitic organization, corresponding to the
243 increased sp^2/sp^3 ratio. In addition, it was found through a theoretical calculation that the binding energy
244 of the PAHs on soot surfaces was closely related to the mass of PAHs in the stack, and small PAHs had
245 lower binding energy relative to the large ones (Herdman and Miller, 2008; Raj et al., 2011). As a result,
246 there is a high probability for amorphous and small PAHs that can escape from the PAHs stacks in soot
247 by overcoming van der Waals force of attraction, which develops a more ordered structure, in line with
248 the current XPS data. An increase in sp^2/sp^3 hybridization ratio corresponds to an enhancement in
249 graphitic planar structures within soot samples, which reduces active sites for oxygen attack and thus
250 lowers soot reactivity (Alfe et al., 2009). A similar finding was reported by Gaddam et al., (2016), who
251 pointed out that the large sp^2/sp^3 hybridization ratio for the model carbon presented low reactivity. Fan et
252 al., (2019) revealed that the diesel soot particles with the large sp^2/sp^3 hybridization ratio presented more
253 resistance to oxidation.

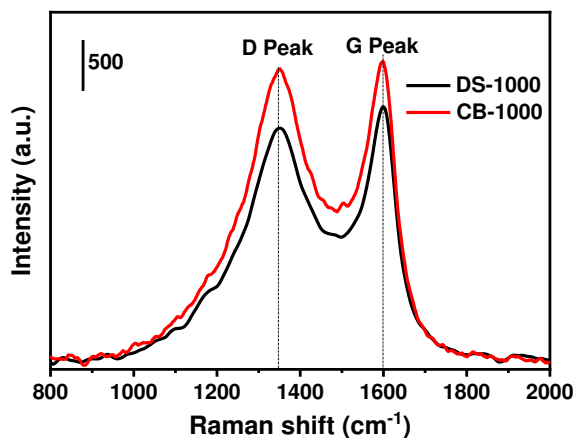
254



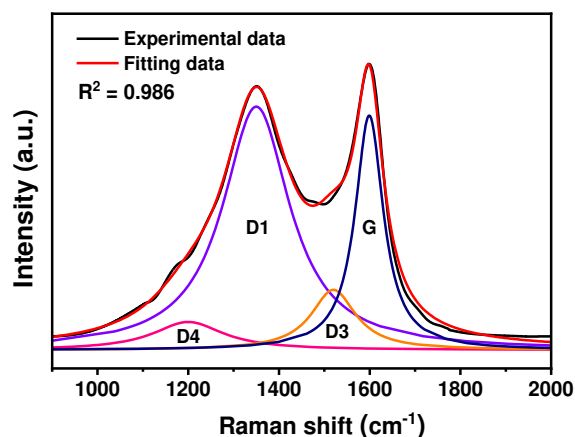
255
256 **Fig. 6.** Sp²/sp³ hybridization ratios as functions of thermal treatment temperature.

257 3.3. Graphitization degree

258 RS was employed to assess the graphitization degree of the soot samples. Fig. 7 shows the
 259 representative baseline-corrected, smoothed spectra of DS-1000 and CB-1000. It can be observed that
 260 these two spectra show two broad peaks at around 1350 cm⁻¹ (D peak) and 1600 cm⁻¹ (G peak). For
 261 quantitative analysis, the spectrum of each soot sample is deconvoluted and fitted by three Lorentzian
 262 functions and one Gaussian function (Seong and Boehman, 2013), as shown in Fig. 8. The Lorentzian
 263 functions refer to the D1 band assigned to the carbon atoms at the edge sites of the graphene layers (Seong
 264 and Boehman, 2011), the D4 band arising from the C=C and C-C bands (Cuesta et al., 1994; Dippel et
 265 al., 1999), and the G band as a result of the ideal graphitic lattice (Seong and Boehman, 2013; Ge et al.,
 266 2019), while the Gaussian function corresponds to the D3 band arising from the amorphous carbon of the
 267 soot (Cuesta et al., 1994; Parent et al., 2016).



268
269 **Fig. 7.** Representative Raman spectra of DS-1000 and CB-1000.



270
271 **Fig. 8.** Four-band fitting of representative Raman spectrum for DS-1000.

272 The peak intensity ratios of the D1 band or the full width at half maximum (FWHM) of the bands to
 273 the G band were frequently employed to determine the graphitization degree of carbon materials (Yoshida
 274 et al., 2006; Sheng, 2007; Zaida et al., 2007). However, only the peak intensity ratio or the FWHM of the
 275 bands is likely unable to be a complete representation of the evolution of soot structural order. By contrast,
 276 the peak area ratio (integrated intensity) is the function of the FWHM and the peak intensity, which
 277 includes the effect of these two parameters. As a result, the peak area ratios of D1 to G (A_{D1}/A_G) are used
 278 to evaluate the graphitization degree of soot samples in the present study. A lower A_{D1}/A_G ratio indicates
 279 a more ordered structure in soot (Tuinstra and Koenig, 1970; Sheng, 2007). Fig. 9 shows the change in

280 graphitization degree of soot samples against various thermal treatment temperatures. Compared to diesel
281 soot, the carbon black is observed to have a lower value of A_{D1}/A_G ratio at the same thermal treatment
282 temperature. For the diesel soot and carbon black, the values of A_{D1}/A_G reduce from 1.89 to 1.59 and from
283 1.85 to 1.56 with the temperature increasing from 600 to 1000 °C, respectively, indicating the
284 transformation towards more-ordered structure for both soot samples. Such a structural transformation is
285 mainly because the amorphous species on the soot surfaces are desorbed during thermal treatment (Sheng,
286 2007; Zaida et al., 2007; Raj et al., 2014). Compared to carbon atoms in the basal plane, the carbon atoms
287 at the edge sites of the graphene were reported to have 100-1000 times more reactive (Marsh and Kuo,
288 1989; Vander Wal and Tomasek, 2004; Vander Wal and Mueller, 2006). The thermally treated soot
289 samples possess more ordering of the soot crystallite structure, corresponding to the lower ratio of edge
290 to base carbon atoms. As a result, soot samples after thermal treatment present more resistance towards
291 oxidation. A similar finding was reported by Sheng (2007), who studied the structure and reactivity of
292 coal chars under different thermal treatment conditions and identified that the thermal deactivation of coal
293 char was dependent on the structural ordering of char crystallite. Feng et al., (2002) probed the change in
294 the structural ordering of coal char during thermal treatment and the effect on its reactivity. The results
295 revealed that the decrease in reactivity during thermal treatment was due to a crystallite-perfecting process.
296 Raj et al., (2014) believed that thermal treatment decreased the number of carbon atoms at the edge sites
297 for reaction, thus lowering soot reactivity.

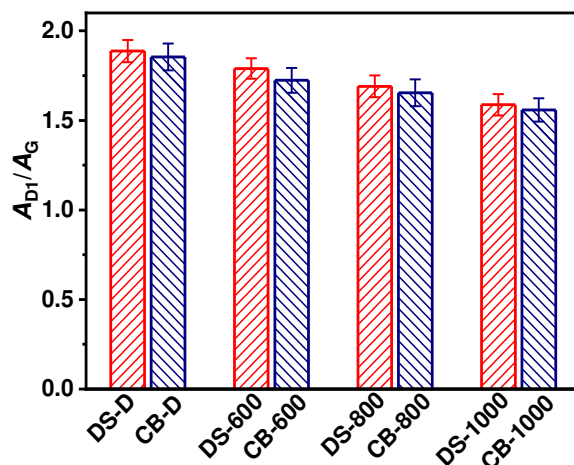


Fig. 9. A_{D1}/A_G ratios as functions of thermal treatment temperature.

298

299

300 Close observation of Figs. 3, 5, 6, and 9 present that considering the uncertainties of aliphatic C–H
 301 groups, oxygenated functional groups, sp^2/sp^3 ratio, and A_{D1}/A_G ratio, it appears to be no significant
 302 difference in the average values among these properties of thermally treated samples. To determine the
 303 statistical differences, the statistical analysis, one-way analysis of variance (ANOVA), was conducted.
 304 For all results, the p values obtained from the statistical analysis are lower than 0.05, suggesting that such
 305 differences are statistically significant. It worth mentioning that the Printex-U in the previous studies was
 306 frequently employed as a surrogate for diesel soot (Vander Wal et al., 2007; Arnal et al., 2012). However,
 307 our current results show that the aliphatic C–H groups, oxygenated functional groups, carbon chemical
 308 state and graphitization degree for diesel soot are statistically different from those for the Printex-U,
 309 which is likely due to a lower proportion in heteroatoms and a higher graphitic order for the Printex-U
 310 (Jaramillo et al., 2015). Additionally, soot properties emitted from a diesel engine are affected
 311 significantly by diesel engine type, engine speed and engine load (Lapuerta et al., 2020). As a result,
 312 whether the Printex-U can be employed as the best surrogate for diesel soot to perform related research
 313 remains to be further studied.

314 **4. Conclusions**

315 Variations in surface functional groups, carbon chemical state and graphitization degree of diesel
316 soot and a commercial carbon black was studied during thermal deactivation. The mass loss of diesel soot
317 and carbon black increases with increasing the thermal treatment temperature, particularly at 1000 °C,
318 around 29 % mass loss can be observed for diesel soot. The concentrations of aliphatic C–H groups, C–
319 OH, C=O, and O–C=O groups reduce for diesel soot and carbon black when increasing thermal treatment
320 temperature, whereas the sp^2/sp^3 hybridized ratio and graphitization degree enhance. These results can
321 provide further evidence for thermal deactivation during thermal treatment. Compared to diesel soot, the
322 commercial carbon black has lower concentrations of aliphatic C–H groups, C–OH, C=O and O–C=O
323 groups and higher graphitization degree and sp^2/sp^3 hybridized ratio at the same thermal treatment
324 temperature. Among oxygenated functional groups, the percentage reduction during thermal treatment is
325 largest for the O–C=O groups due to its worst thermodynamic stability.

326 **5. Acknowledgments**

327 This research is supported by the National Natural Science Foundation of China (No. 52006054),
328 the State Key Laboratory of Engines at Tianjin University (Grant No. K2021-05) and the European
329 Union's project MODALES (grant agreement No. 815189).

330 **6. References**

- 331 Agudelo, J.R., Álvarez, A., Armas, O., 2014. Impact of crude vegetable oils on the oxidation reactivity
332 and nanostructure of diesel particulate matter. *Combustion and Flame* 161, 2904-2915.
- 333 Alfè, M., Apicella, B., Barbella, R., Rouzaud, J.N., Tregrossi, A., Ciajolo, A., 2009. Structure–property
334 relationship in nanostructures of young and mature soot in premixed flames. *Proceedings of the*
335 *Combustion Institute* 32, 697-704.
- 336 Arnal, C., Alzueta, M.U., Millera, A., Bilbao, R., 2012. Influence of water vapor addition on soot

337 oxidation at high temperature. *Energy* 43, 55-63.

338 Bladt, H., Schmid, J., Kireeva, E.D., Popovicheva, O.B., Perseantseva, N.M., Timofeev, M.A., Heister,
339 K., Uihlein, J., Ivleva, N.P., Niessner, R., 2012. Impact of Fe Content in Laboratory-Produced
340 Soot Aerosol on its Composition, Structure, and Thermo-Chemical Properties. *Aerosol Science*
341 *and Technology* 46, 1337-1348.

342 Cain, J.P., Gassman, P.L., Wang, H., Laskin, A., 2010. Micro-FTIR study of soot chemical composition—
343 evidence of aliphatic hydrocarbons on nascent soot surfaces. *Physical Chemistry Chemical*
344 *Physics* 12, 5206.

345 Chung, S.-H., Violi, A., 2011. Peri-condensed aromatics with aliphatic chains as key intermediates for
346 the nucleation of aromatic hydrocarbons. *Proceedings of the Combustion Institute* 33, 693-700.

347 Cuesta, A., Dhamelincourt, P., Laureyns, J., Martínez-Alonso, A., Tascón, J.M.D., 1994. Raman
348 microprobe studies on carbon materials. *Carbon* 32, 1523-1532.

349 Dippel, B., Janderb, H., Heintzenberga, J., 1999. NIR FT Raman spectroscopic study of flame soot.
350 *Physical Chemistry Chemical Physics* 1, 4707-4712.

351 Dobbins, R.A., Fletcher, R.A., Lu, W., 1995. Laser microprobe analysis of soot precursor particles and
352 carbonaceous soot. *Combustion and Flame* 100, 301-309.

353 Dobbins, R.A., Govatzidakis, G.J., Lu, W., Schwartzman, A.F., Fletcher, R.A., 1996. Carbonization Rate
354 of Soot Precursor Particles. *Combustion Science and Technology* 121, 103-121.

355 Fan, C., Song, C., Lv, G., Wei, J., Zhang, X., Qiao, Y., Liu, Y., 2019. Impact of post-injection strategy on
356 the physicochemical properties and reactivity of diesel in-cylinder soot. *Proceedings of the*
357 *Combustion Institute* 37, 4821-4829.

358 Feng, B., Bhatia, S.K., Barry, J.C., 2002. Structural ordering of coal char during heat treatment and its
359 impact on reactivity. *Carbon* 40, 481-496.

360 Fetzer, J.C., 2000. Large (C= 24) polycyclic aromatic hydrocarbons: chemistry and analysis. John Wiley
361 & Sons, .

362 Gaddam, C.K., Vander Wal, R.L., 2013. Physical and chemical characterization of SIDI engine
363 particulates. *Combustion and Flame* 160, 2517-2528.

364 Gaddam, C.K., Vander Wal, R.L., Chen, X., Yezerets, A., Kamasamudram, K., 2016. Reconciliation of
365 carbon oxidation rates and activation energies based on changing nanostructure. *Carbon* 98, 545-
366 556.

367 Ge, H., Ye, Z., He, R., 2019. Raman spectroscopy of diesel and gasoline engine-out soot using different
368 laser power. *Journal of Environmental Sciences* 79, 74-80.

369 Guerrero Peña, G.D.J., Alrefaai, M.M., Yang, S.Y., Raj, A., Brito, J.L., Stephen, S., Anjana, T., Pillai, V.,
370 Al Shoaibi, A., Chung, S.H., 2016. Effects of methyl group on aromatic hydrocarbons on the
371 nanostructures and oxidative reactivity of combustion-generated soot. *Combustion and Flame* 172,
372 1-12.

373 Herdman, J.D., Miller, J.H., 2008. Intermolecular potential calculations for polynuclear aromatic
374 hydrocarbon clusters. *The Journal of Physical Chemistry A* 112, 6249-6256.

375 Ibarra, J., Muñoz, E., Moliner, R., 1996. FTIR study of the evolution of coal structure during the
376 coalification process. *Organic Geochemistry* 24, 725-735.

377 Jaramillo, I.C., Gaddam, C.K., Vander Wal, R.L., Lighty, J.S., 2015. Effect of nanostructure, oxidative

378 pressure and extent of oxidation on model carbon reactivity. *Combustion and Flame* 162, 1848-
379 1856.

380 Kirchner, U., Scheer, V., Vogt, R., 2000. FTIR Spectroscopic Investigation of the Mechanism and Kinetics
381 of the Heterogeneous Reactions of NO₂ and HNO₃ with Soot. *The Journal of Physical Chemistry*
382 *A* 104, 8908-8915.

383 Lapuerta, M., Rodríguez-Fernández, J., Sánchez-Valdepeñas, J., 2020. Soot reactivity analysis and
384 implications on diesel filter regeneration. *Progress in Energy and Combustion Science* 78.

385 Liu, Y., Fan, C., Wang, X., Liu, F., Chen, H., 2022. Thermally induced variations in the nanostructure and
386 reactivity of soot particles emitted from a diesel engine. *Chemosphere* 286, 131712.

387 Liu, Y., Song, C., Lv, G., Cao, X., Wang, L., Qiao, Y., Yang, X., 2016. Surface functional groups and sp
388 ³/sp² hybridization ratios of in-cylinder soot from a diesel engine fueled with n -heptane and n
389 -heptane/toluene. *Fuel* 179, 108-113.

390 Liu, Y., Song, C., Lv, G., Wang, X., Li, N., 2017. Virgin and Extracted Soots in Premixed Methane Flames:
391 A Comparison of Surface Functional Groups, Graphitization Degree, and Oxidation Reactivity.
392 *Energy & Fuels* 31, 6413-6421.

393 Marsh, H., Kuo, K., 1989. Kinetics and catalysis of carbon gasification. *Introduction to carbon science.*
394 Elsevier, pp. 107-151.

395 Matsumoto, K., Tojo, M., Jinnai, Y., Hayashi, N., Ibaraki, S., 2008. Development of compact and high-
396 performance turbocharger for 1,050 C exhaust gas. *Mitsubishi Heavy Industries Technical Review*
397 45.

398 McKinnon, J.T., Meyer, E., Howard, J.B., 1996. Infrared analysis of flame-generated PAH samples.
399 *Combustion and Flame* 105, 161-166.

400 Parent, P., Laffon, C., Marhaba, I., Ferry, D., Regier, T.Z., Ortega, I.K., Chazallon, B., Carpentier, Y.,
401 Focsa, C., 2016. Nanoscale characterization of aircraft soot: A high-resolution transmission
402 electron microscopy, Raman spectroscopy, X-ray photoelectron and near-edge X-ray absorption
403 spectroscopy study. *Carbon* 101, 86-100.

404 Pumera, M., Iwai, H., 2009. Multicomponent metallic impurities and their influence upon the
405 electrochemistry of carbon nanotubes. *The Journal of Physical Chemistry C* 113, 4401-4405.

406 Raj, A., Tayouo, R., Cha, D., Li, L., Ismail, M.A., Chung, S.H., 2014. Thermal fragmentation and
407 deactivation of combustion-generated soot particles. *Combustion and Flame* 161, 2446-2457.

408 Raj, A., Yang, S.Y., Cha, D., Tayouo, R., Chung, S.H., 2013. Structural effects on the oxidation of soot
409 particles by O₂: Experimental and theoretical study. *Combustion and Flame* 160, 1812-1826.

410 Raj, A., Zainuddin, Z., Sander, M., Kraft, M., 2011. A mechanistic study on the simultaneous elimination
411 of soot and nitric oxide from engine exhaust. *Carbon* 49, 1516-1531.

412 Reşitoğlu, I.A., Altinişik, K., Keskin, A., 2014. The pollutant emissions from diesel-engine vehicles and
413 exhaust aftertreatment systems. *Clean Technologies and Environmental Policy* 17, 15-27.

414 Roth, P., Eckhardt, T., Franz, B., Patschull, J., 1998. H₂O₂-assisted regeneration of diesel particulate traps
415 at typical exhaust gas temperatures. *Combustion and Flame* 115, 28-37.

416 Ruiz, F.A., Cadrazco, M., López, A.F., Sanchez-Valdepeñas, J., Agudelo, J.R., 2015. Impact of dual-fuel
417 combustion with n-butanol or hydrous ethanol on the oxidation reactivity and nanostructure of
418 diesel particulate matter. *Fuel* 161, 18-25.

419 Russo, C., Stanzione, F., Tregrossi, A., Ciajolo, A., 2014. Infrared spectroscopy of some carbon-based
420 materials relevant in combustion: Qualitative and quantitative analysis of hydrogen. *Carbon* 74,
421 127-138.

422 Santamaria, A., Mondragon, F., Molina, A., Marsh, N., Eddings, E., Sarofim, A., 2006. FT-IR and ¹H
423 NMR characterization of the products of an ethylene inverse diffusion flame. *Combustion and*
424 *Flame* 146, 52-62.

425 Santamaría, A., Mondragón, F., Quiñónez, W., Eddings, E.G., Sarofim, A.F., 2007. Average structural
426 analysis of the extractable material of young soot gathered in an ethylene inverse diffusion flame.
427 *Fuel* 86, 1908-1917.

428 Santamaria, A., Yang, N., Eddings, E., Mondragon, F., 2010. Chemical and morphological
429 characterization of soot and soot precursors generated in an inverse diffusion flame with aromatic
430 and aliphatic fuels. *Combustion and Flame* 157, 33-42.

431 Schejbal, M., Marek, M., Kubíček, M., Kočí, P., 2009. Modelling of diesel filters for particulates removal.
432 *Chemical Engineering Journal* 154, 219-230.

433 Seong, H.J., Boehman, A.L., 2011. Impact of Intake Oxygen Enrichment on Oxidative Reactivity and
434 Properties of Diesel Soot. *Energy & Fuels* 25, 602-616.

435 Seong, H.J., Boehman, A.L., 2013. Evaluation of Raman Parameters Using Visible Raman Microscopy
436 for Soot Oxidative Reactivity. *Energy & Fuels* 27, 1613-1624.

437 Sheng, C., 2007. Char structure characterised by Raman spectroscopy and its correlations with
438 combustion reactivity. *Fuel* 86, 2316-2324.

439 Song, J., Alam, M., Boehman, A.L., 2007. Impact of alternative fuels on soot properties and DPF
440 regeneration. *Combustion Science and Technology* 179, 1991-2037.

441 Song, J., Alam, M., Boehman, A.L., Kim, U., 2006. Examination of the oxidation behavior of biodiesel
442 soot. *Combustion and Flame* 146, 589-604.

443 Soriano, J.A., Agudelo, J.R., López, A.F., Armas, O., 2017. Oxidation reactivity and nanostructural
444 characterization of the soot coming from farnesane-A novel diesel fuel derived from sugar cane.
445 *Carbon* 125, 516-529.

446 Tandon, P., Rosner, D.E., 1996. Sintering kinetics and transport property evolution of large multi-particle
447 aggregates. *Chemical Engineering Communications* 151, 147-168.

448 Tuinstra, F., Koenig, J.L., 1970. Raman spectrum of graphite. *The Journal of chemical physics* 53, 1126-
449 1130.

450 Vander Wal, R.L., 1998. Soot precursor carbonization: Visualization using LIF and LII and comparison
451 using bright and dark field TEM. *Combustion and Flame* 112, 607-616.

452 Vander Wal, R.L., Bryg, V.M., Hays, M.D., 2010. Fingerprinting soot (towards source identification):
453 Physical structure and chemical composition. *Journal of Aerosol Science* 41, 108-117.

454 Vander Wal, R.L., Bryg, V.M., Hays, M.D., 2011. XPS analysis of combustion aerosols for chemical
455 composition, surface chemistry, and carbon chemical state. *Analytical Chemistry* 83, 1924-1930.

456 Vander Wal, R.L., Bryg, V.M., Huang, C.-H., 2014. Aircraft engine particulate matter: Macro- micro- and
457 nanostructure by HRTEM and chemistry by XPS. *Combustion and Flame* 161, 602-611.

458 Vander Wal, R.L., Bryg, V.M., Huang, C.-H., 2016. Chemistry characterization of jet aircraft engine
459 particulate matter by XPS: Results from APEX III. *Atmospheric Environment* 140, 623-629.

460 Vander Wal, R.L., Mueller, C.J., 2006. Initial Investigation of Effects of Fuel Oxygenation on
461 Nanostructure of Soot from a Direct-Injection Diesel Engine. *Energy & Fuels* 20, 2364-2369.

462 Vander Wal, R.L., Tomasek, A.J., 2004. Soot nanostructure: dependence upon synthesis conditions.
463 *Combustion and Flame* 136, 129-140.

464 Vander Wal, R.L., Tomasek, A.J., Street, K., Hull, D.R., Thompson, W.K., 2004. Carbon nanostructure
465 examined by lattice fringe analysis of high-resolution transmission electron microscopy images.
466 *Applied Spectroscopy* 58, 230-237.

467 Vander Wal, R.L., Yezerets, A., Currier, N.W., Kim, D.H., Wang, C.M., 2007. HRTEM Study of diesel
468 soot collected from diesel particulate filters. *Carbon* 45, 70-77.

469 Wang, H., 2011. Formation of nascent soot and other condensed-phase materials in flames. *Proceedings*
470 *of the Combustion Institute* 33, 41-67.

471 Wang, L., Song, C., Song, J., Lv, G., Pang, H., Zhang, W., 2013. Aliphatic C–H and oxygenated surface
472 functional groups of diesel in-cylinder soot: Characterizations and impact on soot oxidation
473 behavior. *Proceedings of the Combustion Institute* 34, 3099-3106.

474 Xu, L., Lingaswamy, A.P., Zhang, Y., Liu, L., Wang, Y., Zhang, J., Ma, Q., Li, W., 2019. Morphology,
475 composition, and sources of individual aerosol particles at a regional background site of the YRD,
476 China. *Journal of Environmental Sciences* 77, 354-362.

477 Yehliu, K., Armas, O., Vander Wal, R.L., Boehman, A.L., 2013. Impact of engine operating modes and
478 combustion phasing on the reactivity of diesel soot. *Combustion and Flame* 160, 682-691.

479 Yehliu, K., Vander Wal, R.L., Armas, O., Boehman, A.L., 2012. Impact of fuel formulation on the
480 nanostructure and reactivity of diesel soot. *Combustion and Flame* 159, 3597-3606.

481 Yoshida, A., Kaburagi, Y., Hishiyama, Y., 2006. Full width at half maximum intensity of the G band in
482 the first order Raman spectrum of carbon material as a parameter for graphitization. *Carbon* 44,
483 2333-2335.

484 Zaida, A., Bar-Ziv, E., Radovic, L.R., Lee, Y.-J., 2007. Further development of Raman microprobe
485 spectroscopy for characterization of char reactivity. *Proceedings of the combustion institute* 31,
486 1881-1887.

487 Zhou, Q., Wang, Y., Wang, X., Bai, Y., 2022. Experimental investigation into the oxidation reactivity,
488 morphology and graphitization of soot particles from diesel/n-octanol mixtures. *Journal of Environmental*
489 *Sciences* 112, 218-230.

490 Zolin, A., Jensen, A.D., Jensen, P.A., Dam-Johansen, K., 2002. Experimental study of char thermal
491 deactivation. *Fuel* 81, 1065-1075.

492